NeeCo: Image Synthesis of Novel Instrument States Based on Dynamic and Deformable 3D Gaussian Reconstruction

Tianle Zeng, Junlei Hu, Gerardo Loza Galindo, Sharib Ali, Duygu Sarikaya, Pietro Valdastri *Fellow, IEEE*, and Dominic Jones*, *Member, IEEE*

***Abstract*— Computer vision-based technologies significantly enhance surgical automation by advancing tool tracking, detection, and localization. However, Current data-driven approaches are data voracious requiring large high-quality labeled image datasets which limits their application in surgical data science. Our Work introduces a novel dynamic Gaussian Splatting technique to address the data scarcity in surgical image datasets. We propose a dynamic Gaussian model to represent dynamic surgical scenes, enabling the rendering of surgical instruments from unseen viewpoints and deformations with real tissue backgrounds. We utilize a dynamic training adjustment strategy to address challenges posed by poorly calibrated camera poses from real-world scenario. Additionally, we propose a method based on dynamic Gaussians for the generation of annotations for our synthetic data automatically. For evaluation, we constructed a new dataset featuring seven scenes with 14,000 frames of tool and camera motion, as well as tool jaw articulation, with a background of an ex-vivo porcine model. Using this dataset, we synthetically replicate the scene deformation from the ground truth data, allowing direct comparisons of synthetic image quality. Experimental results illustrate that our method generates photo-realistic labeled image datasets with the highest values in Peak-Signal-to-Noise Ratio (29.87). We further evaluate the performance of U-NetPlus and DBH-YOLO models trained on real, synthetic, and mixed synthetic images using an unseen real-world image dataset. Our results show that the performance of models trained on real and synthetic images differs by less than 1.5% across various metrics, while the model trained on the mixed synthetic dataset improves model performances by nearly 15%.**

***Index Terms*— Surgical Data Science, Surgical AI, Data generation, 3D Gaussian splatting, Laparoscopy.**

I. Introduction

COMPUTER vision has the potential to significantly enhance automation and intelligence in minimally invasive procedures such as laparoscopic surgery. Advanced techniques such as real-time tracking, segmentation, and classification of surgical instruments can facilitate intelligent surgical navigation, optimize surgical planning, and enhance overall surgical efficiency and safety [1]. Achieving these goals relies heavily on deep learning-based image understanding methods, such as semantic segmentation and object detection.

Most deep learning-based methods used in surgical data science are supervised, requiring a substantial amount of annotated image data for training to ensure robustness in complex and highly dynamic surgical scenarios. Although semi-supervised, self-supervised, and few-shot learning approaches exist, they often face challenges in achieving the same level of performance as supervised methods [2]. However, the lack of high-quality labeled surgical image datasets has constrained the development of these methods [3]. This scarcity arises from several factors: Ethical concerns in recording surgical videos complicate the management and sharing of medical data, while issues like limited field of view, lens distortion, and frequent obstructions from tools, blood, and smoke during procedures lead to poor image quality and incomplete visual information [4]. These challenges make it difficult to generate high-quality datasets, as detailed annotations require significant time and expertise and are further impacted by annotator subjectivity.

As a result, developing methodologies for addressing data scarcity in laparoscopy has become a key research focus. Using 3D virtual simulators to generate synthetic images [5] and render textures using photo rendering software [6] provides one option. However, these images often lack realism. Alternatively, methods using SLAM techniques [7], [8] reconstruct static surgical scenes. However, the limited capability in generating labels and poor image quality restrict their effectiveness in training robust neural networks. To overcome the challenges of manual annotation and improve image quality, some studies have explored the use of image synthesis [9] and weak annotations [10]. Other works have proposed using generative models and Image-to-Image Translation techniques [11] to generate simulated data for model training. These methods generate realistic images for static scenes but fall short when applied to highly dynamic scenarios such as laparoscopic surgery.

Neural Radiance Fields (NeRFs) [12] and 3D Gaussian Splatting (3DGS) [13] have shown significant potential for image dataset generation. Both methods can handle dynamic

This paper was submitted for review on XXX

T. Zeng, J. Hu, P. Valdastri, and D. Jones are with the STORM Lab UK, School of Electronic and Electrical Engineering, University of Leeds, Leeds, UK. (e-mail:D.P.Jones@leeds.ac.uk). G. L.Galindo, S. Ali, D. Sarikaya are with the STORM Lab UK, School of Computing, University of Leeds, Leeds, UK.

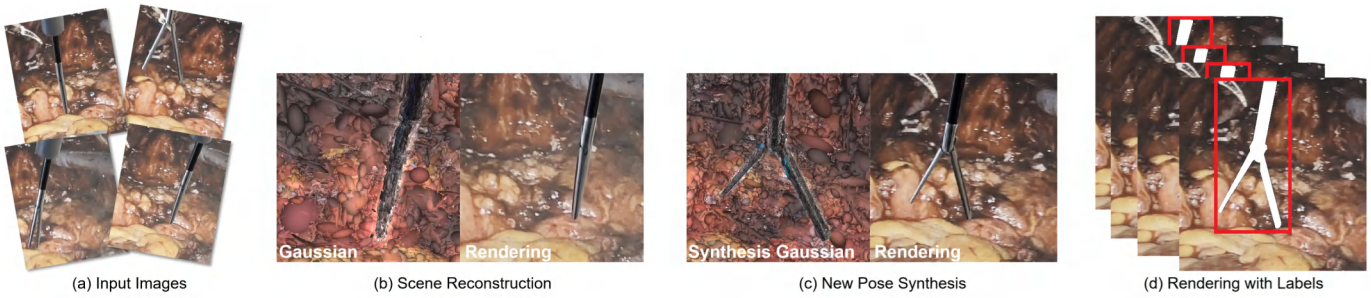

(a) Input Images (b) Scene Reconstruction (c) New Pose Synthesis (d) Rendering with Labels

Fig. 1. **Method Overview.** (a) Our method takes images of surgical instruments in various poses as input. (b) Then we reconstruct the 3D Gaussian representation of the surgical scene. (c) After the reconstruction, our method can predict the 3D Gaussian representation of unseen deformations of the surgical instruments. (d) We render them as realistic images, and additionally can obtain the tool annotations automatically. In (d) the red boxes indicate the bounding boxes, and the white areas represent the instrument segmentation masks.

scenes, and recent approaches that combine NeRFs or 3DGS with time-dependent neural displacement fields [14], [15] have become representative works in dynamic surgical scene reconstruction. Compared to NeRF, 3DGS has an advantage in reconstruction, enabling explicit scene representation and offering scene-editing capabilities that NeRF lacks. This makes 3DGS more suitable for reconstructing dynamic surgical scenes and generating corresponding image data. However, it still faces several challenges.

Firstly, 3DGS-based methods excel with simulated datasets due to access to ground truth camera poses and scene point clouds. However, their performance deteriorates on real-world datasets [16] due to reliance on Structure-from-Motion (SfM) for camera pose calibration. In dynamic scenes, object movement and deformation cause significant initialization errors, as SfM struggles to match frames and register points accurately [17], severely impacting 3DGS training. Moreover, these methods cannot handle dynamic scenes with surgical instruments, focusing instead on visualizing tissue deformations. This limits their applicability for tasks like instrument detection, segmentation, and pose estimation, which are crucial for surgical automation. Additionally, they only learn observed deformations and cannot generate novel ones or annotated data, requiring manual annotation for neural network training. To overcome these challenges, we propose NeeCo, a novel method for generating realistic surgical image datasets based on 3DGS. Our contributions can be summarized as follows:

1.**Novel Dynamic Surgical Instrument Reconstruction Framework:** We propose an innovative framework that synthesizes novel scenes of kinematically-posable surgical instruments, learned from previously observed images of recorded instrument kinematics (position, rotation, and jaw aperture angle). This framework can reconstruct instruments in dynamic surgical scenes and predict the view under tool movement, including unseen pose and position changes for instruments.

2.**Dynamic Adjustment Method for 3DGS Training:** We introduce a method for dynamically adjusting the 3DGS training process. We do this by adopting different training strategies at various stages. Our approach addresses the challenges posed by poor initialization from inaccurate camera poses when using our recorded surgically relevant scenes of ex-vivo porcine organs as input.

3.**Automatic Generation of Annotations:** The proposed method can automatically generate annotation information alongside the rendered images without human intervention based on the dynamic Gaussian kinematic changing.

4.**Evaluation with Ground Truth (GT) Images of Anatomy:** We record a new dataset using ex-vivo abdominal organs from a porcine model while tracking our tool state, producing GT images and data that can be directly compared with our generated images. Through comparative experiments on image quality and neural network training using GT images as the benchmark, we ensure the reliability of our conclusions and show a marked increase in synthesis quality and compared with comparable SOTA methods.

II. Related Work

This section examines significant advancements in surgical scene reconstruction, focusing on traditional, implicit, and explicit representation methods. Given that our approach emphasizes the reconstruction and representation of surgical scenes that include instruments, we also review current methodologies for surgical instrument synthesis in medical imaging.

A. Surgical Scene Reconstruction

1) Traditional Representation: Early studies, such as [7], [8] relied on stereo inputs to recover scene depth information through SLAM techniques. These methods generated depth maps via depth estimation and fused the depth maps from multiple viewpoints in 3D space to achieve static scene reconstruction. Subsequent advancements, such as [18] and [19], introduced new stereo depth estimation frameworks by tracking the deformations of key points in the scene, enabling simple 3D deformable reconstruction. These methods heavily rely on sparse deformation fields for tracking deformations and are limited when faced with complex or significant deformations, capturing only relatively small changes. Additionally, the overall quality of the images generated by these methods is often subpar, further limiting their effectiveness in training robust neural networks.

2) Implicit Representation: Implicit representations, such as NeRF [12], have significantly advanced medical imaging. Unlike traditional methods that rely on spatial geometric information and the tracking of key deformation points for reconstruction, implicit representations use neural radiance

fields and deformation fields to capture and represent scene deformation. This combination facilitates the effective reconstruction of dynamic scenes. Recently, EndoNeRF [15] has emerged as a promising solution for dynamic surgical scene reconstruction. It uses tool-guided ray casting, stereo depth-cueing ray marching, and stereo depth-supervised optimization to achieve high-quality results but suffers from lengthy training times. To address this, Forplane [20] optimizes training by conceptualizing surgical procedures as 4D volumes, decomposed into static and dynamic fields with orthogonal neural planes, reducing memory usage and accelerating optimization. However, these methods neglect the modeling of surgical instruments and produce non-editable, limited generalization scenes.

3) Explicit Representation: Explicit scene reconstruction methods, such as 3DGS [13], overcome the limitations of implicit representation methods, which are difficult to edit. By manipulating the obtained scene 3D Gaussian, it is possible to rotate and translate objects within the scene without sacrificing reconstruction quality. Additionally, these methods enable rapid training and real-time rendering of the reconstructed scenes. Similar to EndoNeRF [15], EndoGaussian [14] and EndoGS [21] use 3D Gaussians to represent surgical scenes. These methods process ordered images with continuous deformations over time, segmenting them into static scenes and introducing time-based deformation fields to stitch them together, reconstructing tissue deformations in dynamic surgical scenarios. However, they face significant challenges: they struggle to accurately capture surgical instrument deformations, can only reconstruct past scenes without predicting future changes, and demand high-quality input data, including continuous temporal changes and precise camera poses.

B. Instrument Synthesis in Medical Imaging

Various methods have been developed to generate surgical instrument images. Game engines and surgical simulators [22], [23] provide scalable, noise-free solutions that automatically generate annotations. However, the synthetic images produced by these methods often lack realism, failing to accurately replicate the lighting and textures of real scenes, which can negatively impact the generalizability of models trained on such data. Generative neural networks like GANs and CycleGANs [24], [25], [26] can create synthetic datasets that closely resemble real image distributions, achieving higher image quality. However, these methods can typically only generate pseudo annotations for tasks like segmentation, and they often fall short of providing the high-quality, accurate annotations required for supervised learning. Recent approaches [27], [28] have attempted to integrate simulation environments with generative networks, enhancing simulated medical images with real image characteristics to produce high-quality, annotated synthetic datasets. Nevertheless, these methods are primarily designed for static scenes and struggle to modify the pose, orientation, and deformation of instrument end-effectors, which limits their effectiveness in dynamic surgical environments.

III. Methodology

We propose a method for synthesizing realistic images of surgical instruments exploiting the recent advances in 3D Gaussian Splatting. Our approach allows for dynamic selection of both the user's viewpoint and the instrument's kinematic state (6-DoF pose and jaw aperture angle), allowing for a user to train a 3DGS model on a limited size dataset before synthesizing supplemental images to enhance the performance of neural networks trained on the data. Our model is trained from a monocular video of a moving surgical instrument in a surgical scene; each frame is recorded with kinematic information of the tool's current state. From this, we train a deformable Gaussian model using an MLP to decode user-specified instrument states. Our approach utilizes multiple enhancements to the training method of deformable Gaussian models, namely dynamically adjusting the training rates of the Gaussian's properties, uniform motion rendering, and dynamic compensation of camera poses. We also use our trained Gaussian model to automatically generate segmentation masks and relevant instrument bounding boxes before proving the quality of our image synthesis to enhance the performance of AI-based tool detection and segmentation.

A. Preliminary: 3D Gaussian Splatting

3DGS utilises a field of explicitly defined Gaussians in 3D space to define and render a 2D scene [13]. We initialize our 3D Gaussians from point clouds generated by COLMAP [29], following the specified mathematical expression:

$$G(x) = e^{-\frac{1}{2}(\boldsymbol{x}-\boldsymbol{\mu})^T \boldsymbol{\Sigma}^{-1}(\boldsymbol{x}-\boldsymbol{\mu})} \tag{1}$$

where $\boldsymbol{\mu}$ denotes the mean value of the point cloud $P(x, y, z)$ and $\boldsymbol{\Sigma}$ is a 3D covariance matrix, expressed as $\boldsymbol{\Sigma} = \boldsymbol{RSS^T R^T}$. Here, $\boldsymbol{R}$ denotes a 3×3 rotation matrix, and $\boldsymbol{S}$ is a 3×3 diagonal matrix representing the scale. To simplify its representation, the rotation matrix $\boldsymbol{R}$ is converted into a vector $\boldsymbol{r}$. These 3D Gaussians are projected into 2D and rendered for each pixel using the following 2D covariance matrix Σ':

$$\boldsymbol{\Sigma'} = \boldsymbol{JW\Sigma W^T J^T}, \tag{2}$$

where $\boldsymbol{J}$ is the Jacobian of the affine approximation of the projective transformation, $\boldsymbol{W}$ is the view matrix transitioning from world to camera coordinates, and $\boldsymbol{\Sigma}$ denotes the 3D covariance matrix.

The color of the pixel on the image plane, denoted by $\mathbf{C}$, is calculated by α-blending the contributions of the N Gaussians, which are sorted from closest to farthest:

$$\mathbf{C} = \sum_{i \in N} \alpha_i c_i \prod_{j=1}^{i-1} (1 - \alpha_j) \tag{3}$$

$$\alpha_i = \sigma_i e^{-\frac{1}{2}(\boldsymbol{\mu}-u_i)^T \Sigma' (\boldsymbol{\mu}-u_i)} \tag{4}$$

where c_i represents the color of each Gaussian along the ray, and u_i denotes the uv coordinates of the 3D Gaussians projected onto the 2D image plane.

During initialization, the Gaussian is also assigned an opacity attribute σ, thus the 3D Gaussian is defined as:

$$G(\boldsymbol{\mu}, \boldsymbol{r}, \boldsymbol{s}, \sigma) \tag{5}$$

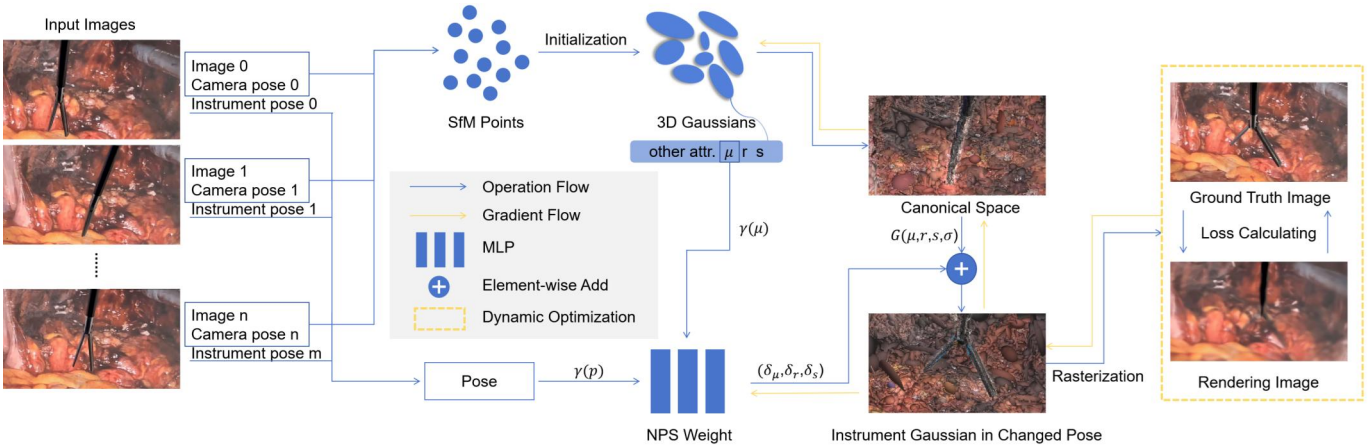

Fig. 2. **Training Process Overview.** Given a set of unordered images of a laparoscopic surgery procedure, our method represents the dynamic scene using 3D Gaussians. It synthesizes the Gaussian representation of the instrument in a new pose from novel viewpoints. The standard 3D Gaussian scene representation is trained in a canonical space. An MLP estimates the attribute changes during scene deformation, transforming the canonical Gaussians to the new deformation. The transformed Gaussians are then rendered using rasterization. The rendered images are compared with ground truth images to evaluate the training. The entire training process is optimized using a dynamic optimization strategy.

B. Deformable Gaussian Splatting

When part of the scene undergoes deformations, the Gaussian properties in the deformation regions are varied to represent the new state, expressed as:

$$G'(\boldsymbol{\mu}', \boldsymbol{r}', \boldsymbol{s}', \sigma') = G(\boldsymbol{\mu} + \delta\boldsymbol{\mu}, \boldsymbol{r} + \delta\boldsymbol{r}, \boldsymbol{s} + \delta\boldsymbol{s}, \sigma + \delta\sigma) \quad (6)$$

To mitigate the impact of dynamic changes in the scene, we train this standard Gaussian model in the canonical space. To decode from our canonical model $\mathcal{C}$, we use an MLP to model the required parametric change in $\boldsymbol{\mu}, \boldsymbol{r}$, and $\boldsymbol{s}$ for each Gaussian, referred to as the New Pose Synthesis (NPS) weight $\mathcal{F}$, with depth and hidden layer size of $D = 12$ and $W = 256$, respectively. The NPS weight takes two inputs: a representation of object movement in the scene, $\mathbf{p}$, and the coordinates of the Gaussian centers in the previous frame, $\boldsymbol{\mu}$. The parameter $\boldsymbol{\mu}$ primarily represents positional changes (translation), while $\mathbf{p}$, which includes the rotation and jaw aperture change of the laparoscopic instrument, captures the instrument's deformation. Together, these two parameters effectively represent the scene's deformations. We use a positional encoder (γ) on both $\mathbf{p}$ and $\boldsymbol{\mu}$ (adapted from [12]) to enhance training quality, where:

$$\gamma(\boldsymbol{\mu}) = (\sin(2^k \pi \boldsymbol{\mu}), \cos(2^k \pi \boldsymbol{\mu}))_{k=0}^{L-1} \quad (7)$$

Resulting in:

$$(\delta\boldsymbol{\mu}, \delta\boldsymbol{r}, \delta\boldsymbol{s}) = \mathcal{F}(\gamma(\boldsymbol{\mu}), \gamma(p)) \quad (8)$$

And giving the final representation of the synthesised scene as:

$$G' = \mathcal{C} + \mathcal{F}(\gamma(\boldsymbol{p}), \gamma(\boldsymbol{\mu})) \quad (9)$$

We do not update the opacity σ during this process, as it primarily affects the rendering process by determining the final rendered color. Since instruments typically keep to a constant colour space regardless of pose, we do not estimate the opacity. Nevertheless, σ of the Gaussian in the canonical space is still optimized during training.

It is worth noting that methods like 4DGS [30] and D-3DGS [16] also use MLPs to model dynamic scenes. However, in these methods, the primary aim of the MLP is to decouple continuous dynamic scenes into multiple static scenes. The MLPs in these methods use a time parameter t to reconstruct learned scenes within the timeframe of the parent video. In essence, they do not treat the dynamic scene as a whole; instead, the MLP learns the Gaussian representation of each decoupled static scene individually, requiring the input data to be temporally continuous and within range of the training data. In contrast, the MLP in our approach is designed to predict changes in Gaussian attributes based on object movement, training and learning from the dynamic scene as a whole. Consequently, our method can handle unordered image inputs and generate scenes from object movement outside of the observed values.

C. Deformable Gaussian Training

The input is unordered images that capture a dynamic surgical scene with instrument deformation. Initially, we use SfM to calibrate the camera pose and generate a sparse point cloud representing the scene, along with the object movement parameter $\boldsymbol{p}$ for each frame. The sparse point cloud is then initialized into Gaussians and transferred into the canonical space for training. As the scene transitions from between frames, the Gaussian attributes $\boldsymbol{\mu}$ and $\boldsymbol{p}$ of the current frame are encoded and fed into the NPS weight, which attributes necessary to transform the Gaussians from the current frame to the next.

As training progresses, the NPS weight gradually learns to induce changes in the scene's Gaussian representation. As this is built from changes in $\boldsymbol{\mu}$ and $\boldsymbol{p}$ between two frames, we can generate new frames by inputting arbitrary $\boldsymbol{\mu}$ and $\boldsymbol{p}$ values. We further validate this ability to generate high-quality Gaussians representing unseen scene transformations in the experimental section IV. Following the 3DGS [13], we render the transformed scene's Gaussians into an image. This

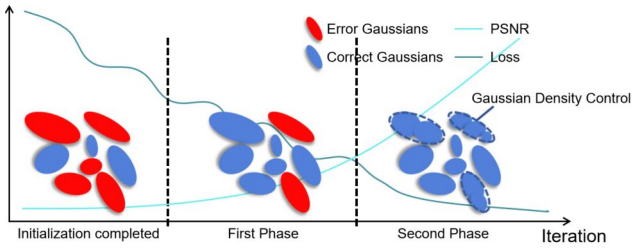

Fig. 3. **Dynamic Density Control.** In the first phase of training, the Gaussian distributions are newly initialized and contain numerous error points. During this phase, the loss function shows fluctuations, and the PSNR values are low but steadily increasing. In the second phase, the density control is gradually relaxed throughout the iterations, allowing for the splitting and cloning of Gaussian points to further enhance the training quality.

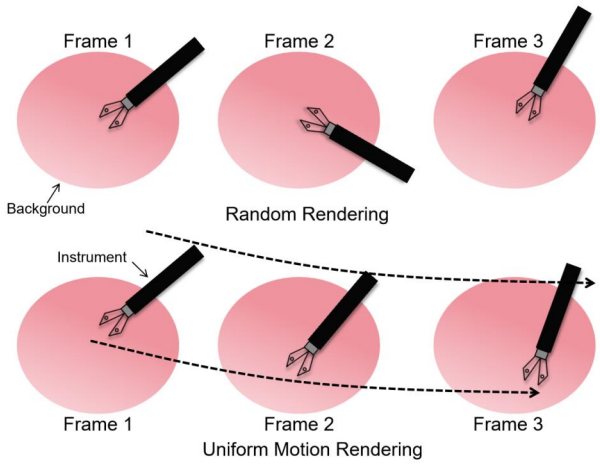

Fig. 4. **Uniform Motion Rendering:** The first row shows random rendering, where the instrument undergoes significant changes between frames. The second row shows uniform motion rendering, where the instrument's movement between frames is more consistent.

rendered image is then compared with the ground truth image of the transformed scene to calculate the loss function $\mathcal{L}$, a combination of $\mathcal{L}_1$ loss and a D-SSIM term:

$$\mathcal{L} = (1-\lambda)\mathcal{L}_1 + \lambda\mathcal{L}_{\text{D-SSIM}} \tag{10}$$

It is important to note that the rendering process heavily depends on accurate camera poses. SSIM (Structural Similarity Index Measure) is sensitive to spatial relationships within the image, and viewpoint discrepancies can lead to significant visual differences and cause SSIM to drop sharply. Therefore, we assign a higher weight $(1-\lambda = 0.9)$ to the $\mathcal{L}_1$ term, reducing the weight of the $\mathcal{L}_{\text{D-SSIM}}$ term and minimizing the impact of camera pose errors on the training outcome. After calculating the loss, we update the attributes of the Gaussians in the canonical space and all NPS weight parameters. Fig. 2 summarizes our training process.

D. Dynamic Training Adjustment

1) Dynamic Density Control Adjustment: Density control is essential to the 3DGS pipeline; it enhances scene detail by cloning small Gaussians in sparse areas and splitting large ones in dense areas. It is predefined before training by three parameters: the densification interval P_{di}, the opacity reset interval P_{oi}, and a positional gradient threshold τ_{pos}. It is, however, particularly sensitive to initialization errors. Incorrect camera poses introduce numerous erroneous points into the initialized Gaussian models, and density control can exacerbate these errors by misplacing or redundantly multiplying error-prone Gaussians, eventually causing training failure. While 3DGS can correct errors in static scenes, its robustness is compromised with dynamic datasets, as premature density control amplifies errors beyond its corrective capabilities. These fixed parameters do not accommodate the rapid dynamics of real-world scenes. Removing or delaying density control can mitigate these issues but may compromise the overall quality of the Gaussian representation, as density control is crucial for enhancing fidelity and detail.

We propose an adaptive density control strategy, illustrated in Fig. 3. We partition the training into two phases, guided by reductions in the loss function and improvements in the Peak Signal-to-Noise Ratio (PSNR) of rendered images, and dynamically adjust the density control during the training process. Existing works [31], [32] also explored the density control module in Gaussian Splatting, focusing on enhancing image detail. However, they do not address the negative impact of erroneous initialization on the training process.

In the first phase, Gaussians are newly initialized and often contain numerous errors. During this initial phase, we restrict density control to prioritize correcting these erroneous points to their accurate positions. We extend densification and opacity reset intervals and increase the gradient threshold, setting $P_{di} = 500$, $P_{oi} = 10,000$, and $\tau_{pos} = 0.0004$. Once the erroneous points are largely corrected in the first phase, the second phase commences as PSNR values exceed 20 and the loss function consistently declines. Here, we reintroduce density control, enhanceing geometric detail and refines overlapping areas, significantly improving model accuracy and robustness. Parameters for this phase are set to $P_{di} = 200$, $P_{oi} = 3000$, and $\tau_{pos} = 0.0002$.

2) Dynamic Spherical Harmonics Function Update: Similar to dynamic density control, we adopt an adaptive strategy for updating Spherical Harmonics (SH) coefficients. SH captures illumination, and details in complex scenes, with higher-order SH coefficients, representing finer details but resulting in increased training complexity. In the early training stages, we restrict SH updates to lower orders, focusing on correcting erroneous Gaussian initialization rather than complex details to reduce computational overhead and accelerate convergence (primarily learning basic lighting and geometric structure). As training progresses, we increase the order of SH updates to capture more complex details, learn finer variations in lighting and scene details, and improve overall rendering performance. This strategy ensures initial stability and fully leverages higher-order SH's expressive power for high-precision scene reconstruction.

3) Uniform Motion Rendering: In the original 3DGS training process, input images are randomly selected during training. However, since our input images include different instrument poses, randomly selected images present significant variations in the instrument's appearance between two consecu-

tive images. An instrument part visible in one frame might become occluded in the next. These substantial variations pose challenges for the NPS Weight to accurately predict Gaussian changes in the early stages of training, causing a larger computed loss and slowing down the convergence of the training process.

To address this issue, we introduce uniform motion simulation as shown in Fig. 4. In the first training phase, we sort the images according to the pose positions of the instrument, simulating a uniform motion with slow changes. These smaller object motions ($\boldsymbol{p}$) are easier to learn, enabling the training process to converge more quickly. Once the training progresses to the second phase, we revert to the random rendering strategy, allowing the model to adapt to larger variations in the instrument's poses. Gradually introducing larger variations helps the NPS learn and adapt to complex changes in the instrument, thereby enhancing the overall performance and robustness of the model.

4) Dynamic Camera Pose Compensation: Training with imprecise poses may negatively impact the training process. Inaccurate camera poses in real-world datasets can cause spatial jitter between frames in the test or training set, resulting in significant deviations between the rendered test images and the ground truth [33]. We propose a compensation mechanism for the rendering jitter caused by inaccurate camera poses. Previous works [16], [34] either directly compensate for camera poses using estimates from visual-inertial odometry (VIO) or are specifically designed for tasks involving temporal interpolation. In contrast, our compensation method can adapt to errors introduced by camera movements in all directions and is applicable in stages, aligning seamlessly with the dynamic training process outlined in this work. This compensation primarily occurs in the first phase of training:

$$(\delta\boldsymbol{\mu}, \delta\boldsymbol{r}, \delta\boldsymbol{s}) = \mathcal{F}(\gamma(\boldsymbol{\mu}), \gamma(\boldsymbol{p}) + \Delta) \tag{11}$$

$$\Delta = (\mathcal{N}(0,1) - 0.5) \cdot \beta \cdot t_{phase} \tag{12}$$

where Δ represents the compensation, $\mathcal{N}(0,1)$ denotes the standard Gaussian distribution, and subtracting 0.5 adjusts the value range from $[0,1]$ to $[-0.5, 0.5]$. This adjustment allows for the simulation of camera pose errors in both positive and negative directions. The scaling factor β is empirically determined and has a value of 0.3. t_{phase} is a boolean value used to determine the current training phase; it is set to 1 during the first phase and 0 during the second phase.

E. Automatic Annotation Generation

We generate dataset annotations in two steps. First, we generate a segmentation mask, and second, we use this to define a bounding box for detection. When instrument movement occurs, Gaussians (G) in the scene may be represented as $G'(\boldsymbol{\mu}+\delta\boldsymbol{\mu}, \boldsymbol{r}+\delta\boldsymbol{r}, \boldsymbol{s}+\delta\boldsymbol{s}, \sigma)$. When rendered with a new pose, the NPS weights $(\delta\boldsymbol{\mu}, \delta\boldsymbol{r}, \delta\boldsymbol{s})$ for the instrument (the moving part of the scene), are much greater than those observed in the background (mainly static). To identify significant changes, we experimentally establish a variation threshold $\mathcal{H}_{\delta\boldsymbol{\mu}}, \mathcal{H}_{\delta r}, \mathcal{H}_{\delta s}$. If the increment in Gaussian attributes exceeds this threshold, we consider it indicative of substantial deformation, labelling these Gaussians as constituents of the instrument.

By rendering only the Gaussians corresponding to the surgical instrument, we can effectively generate a segmented image of the tool: the background is devoid of Gaussians and will consequently be rendered black, while the instrument is colored as normal (with some artifacts around the edges as a result of low opacity regions of the perimetric Gaussians. We set a threshold of the pixel's RGB magnitude on this segmented rendered image, generating a binary segmentation mask. With this mask, we can automatically generate minimum bounding boxes using the mask's outer contour and bounding boxes using the extremity pixel coordinates.

IV. Experiment

A. Data Recording and Experimental Setup

1) Dataset Collection: Due to the lack of publicly available datasets suitable for our method, which requires simultaneous camera movement and 7-DoF instrument kinematics, we have constructed an experimental platform for data collection. Our experimental setup consists of a laparoscope (Endoskill, MedEasy, China), laparoscopic instruments (MedEasy, China), an electromagnetic (EM) tracking system (Aurora, NDI, Canada), allowing 6-DoF motion tracking of the instrument and laparoscope. Additionally, we modified the instrument handle with a Hall-effect sensor to measure the jaw opening angle. Fig. 5 shows the data recording platform.

We used ex-vivo pig tissue and organs during data collection to create a more realistic surgical environment. Organs were harvested from pigs reared and slaughtered for the food chain. We collected data from various tissues and organs, including the liver, stomach, and colon. These tissues and organs exhibit different visual characteristics such as color, texture, and shape, effectively simulating different surgical environments within the human abdomen. During recording, we used the EM tracker and jaw angle sensor to capture the 7-DoF data of the surgical tools and the camera's 6-DoF pose. We exclusively utilized lighting sources from the laparoscope to achieve a more realistic simulation of real-world surgical scenarios.

Our Gaussian model training dataset consists of three videos, each of a subject organ from our ex-vivo experimental setup (colon, liver, stomach), containing 576000 frames with associated instrument states. To avoid redundancy, we sampled 14000 frames which were used as a training and validation set for training the segmentation and detection Neural Networks. We collected an additional dataset as a test set. This dataset contains 300 images featuring various backgrounds, instrument poses, and deformations not seen in our training data.

2) Implementation Details: We implement our Gaussian model training pipeline using Pytorch. All Gaussian models were trained on an NVIDIA RTX Ada 4500 graphics card and Intel Xeon W5-2455X CPU. Aside from those set by our Dynamic Training Adjustment, all other training parameters are set based on the initial 3DGS work.

We train our Neural Network evaluators on an NVIDIA RTX 4050(6G) graphics card and Intel i7-12650H CPU. All models were trained using their default parameters for 300 epochs.

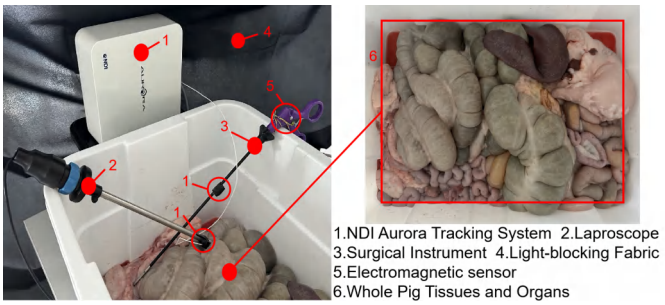

Fig. 5. Data recording platform.

3) Evaluation Metrics: For our image quality comparison, we render full images to compare against the GT. Therefore, we utilize three comparative evaluation metrics that compute similarity over the full image: SSIM, PSNR, and LPIPS, typically used within synthetic image generation [13], [16], [35]. For our Neural Network evaluators, we use Precision and Recall for object detection and IoU and Dice for segmentation. To mitigate the effect of randomness on model performance evaluation, we conduct multi-fold experiments for each model.

B. Image Quality Experiment

Our image quality experiments evaluated the images rendered by the proposed method, comparing them with the GT (the last three images in Fig. 6). We replicate our GT images by inputting the GT 7-DoF data, allowing the model to render the identical scene as observed in the GT images (column 1 in Fig.6). We overlaid the rendered images with the GT images to generate PSNR difference maps, visualizing the discrepancies between them. As shown in Fig.6, the red areas, indicating discrepancies, are primarily located in the detailed regions of the surgical tool jaw and the image edges.

We selected several state-of-the-art (SOTA) methods for comparison, including 3DGS [13], NeRFies [35], 4DGS [30], and D-3DGS [16]. Due to the inability of 4DGS [30] and D-3DGS [16] to function properly on our collected real-world dataset (due to inaccurate camera poses calibration from SfM), we incorporated the dynamic density control III-D.1 from our proposed method into these two methods to ensure they could operate on our dataset. The rendering results of all the comparison methods are visualized in Fig. 7. Table I summarizes the quantitative results on different datasets.

As shown in Table I, the rendered images from our proposed method outperform the SOTA methods across various evaluation metrics on different background datasets. Moreover, our method achieves satisfactory results even for unseen deformations. From Fig. 7, it can be observed that, although the proposed method exhibits some blurring in certain background regions, it excels in rendering surgical instruments, with both the main body and jaw rendered clearly and closely resembling the GT images.

3DGS [13] struggles to accurately render static surgical tools in dynamic scenes, while NeRFies [35] can only partially render surgical instruments, producing blurry and unrecognizable results. NeRFies' reliance on highly accurate camera poses, which are difficult to obtain in real-world settings, leads to poor performance with inaccurate poses. With the implementation of our Dynamic Density Control, 4DGS [30] and D-3DGS [16] could be applied to real-world datasets, but their rendering quality remained inferior to our proposed method.

C. Neural Network Training Experiment

In our neural network training experiments, we validate the effectiveness of the proposed method using rendered images for training neural networks. We focus on two common downstream tasks in RAMIS: object detection and semantic segmentation. We employ well-established and widely-used models in the respective domains: YOLOv5 [36] for object detection and U-Net [37] for semantic segmentation. Additionally, to align with domain-specific benchmarks in medical imaging, we utilize SOTA neural networks specifically designed for surgical tool detection and segmentation. Specifically, we incorporate DBH-YOLO [38] for object detection and U-NetPlus [39] for semantic segmentation, leveraging our automatically generated labels.

We train six versions of each model from different source datasets: 1. real images with GT pose, 2. real image augmented by standard data augmentation [40]. 3 & 4. synthetic rendering by D-3DGS [16] & 4DGS [30], respectively, 5. synthetic NeeCo rendering of the GT pose, 6. a mix of NeeCo rendered GT pose and new unseen poses. Each dataset contains 1780 images.

Table II summarizes the performance of different models. Overall, with both DBH-YOLO and U-NetPlus, the GT and Render models differ by less than 1.5% in performance metrics, while the mixed synthetic model shows nearly a 15% improvement over the GT model. For DBH-YOLO, the GT (REAL) and Render (NeeCo) models show similar performance, indicating that networks trained on Render images can match those trained on GT images. Models trained using standard augmentation methods (AUGMENT) show performance improvements by rotating or translating the GT images. This helps them handle certain new deformations in the test dataset but are limited in introducing novel views and unseen deformations, leading to only marginal improvements. Although D-3DGS and 4DGS can synthesize new viewpoints, their performance lags due to lower image quality. The mixed synthetic model (NeeCo + Real Images) outperforms both, as it benefits from unseen deformations and varied camera viewpoints, enhancing training diversity and overall performance, Additionally, the standard augmentation methods can be applied to this model to further boost performance. The conclusions for U-Net mirror those drawn from DBH-YOLO. Similar conclusions can be drawn for YOLOv5 and U-Net.

D. Ablation Study

1) Dynamic Density Control and Uniform Motion Rendering: In this section, we evaluate the impact of Dynamic Density Control and Uniform Motion Rendering on the training process. First, we compared the effects of dynamic density control with other density control strategies on training. As illustrated in Figure 8 during the initial training phase, both (a) and (b)

TABLE I
QUANTITATIVE RESULT OF THE COMPARISON EXPERIMENT

Methods	Liver			Stomach			Bowel		
	PSNR ↑	SSIM ↑	LPIPS ↓	PSNR ↑	SSIM ↑	LPIPS ↓	PSNR ↑	SSIM ↑	LPIPS ↓
3DGS [13]	18.01	0.708	0.643	17.21	0.701	0.553	18.33	0.722	0.631
NeRFies [35]	23.12	0.772	0.493	22.17	0.763	0.441	21.71	0.714	0.512
4DGS [30]	25.23	0.847	0.411	25.41	0.837	0.391	23.41	0.786	0.428
D-3DGS [16]	24.01	0.811	0.462	23.32	0.803	0.422	24.68	0.835	0.431
Unseen Deformation	27.52	0.881	0.353	27.01	0.855	0.301	27.81	0.868	0.337
NeeCo	**28.88**	**0.902**	**0.273**	**29.81**	**0.893**	**0.274**	**29.87**	**0.913**	**0.281**

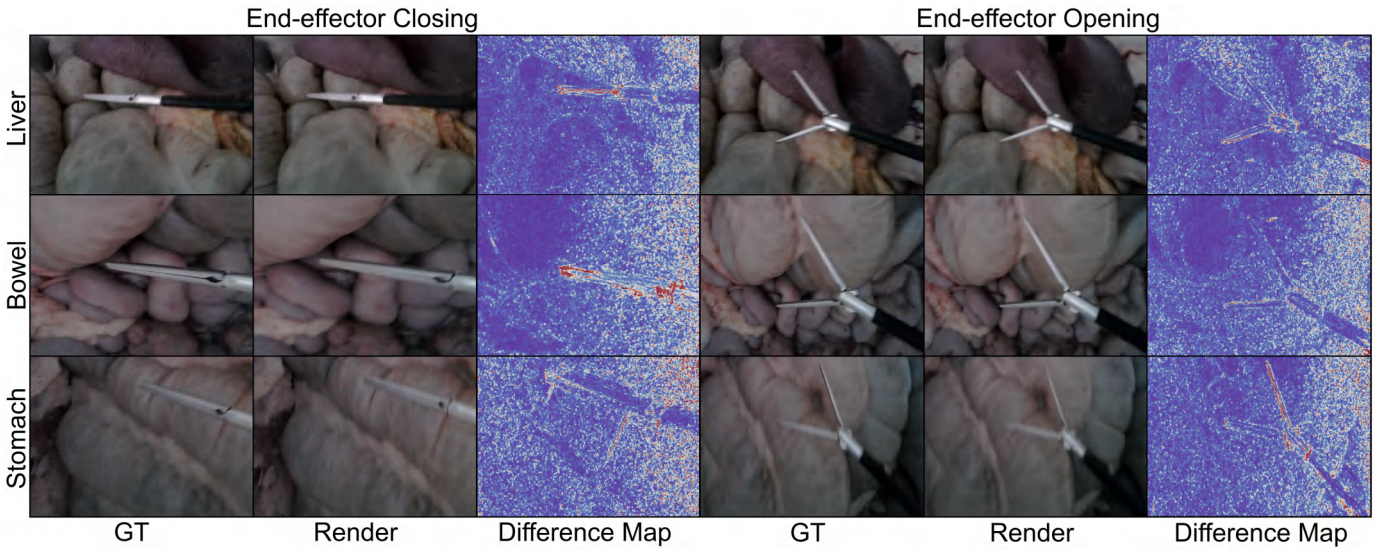

Fig. 6. Reconstruction result with difference maps. From left to right are the GT image, the rendered image, and the difference map. The difference map is created by overlaying the two images, with warm colors indicating areas of difference.

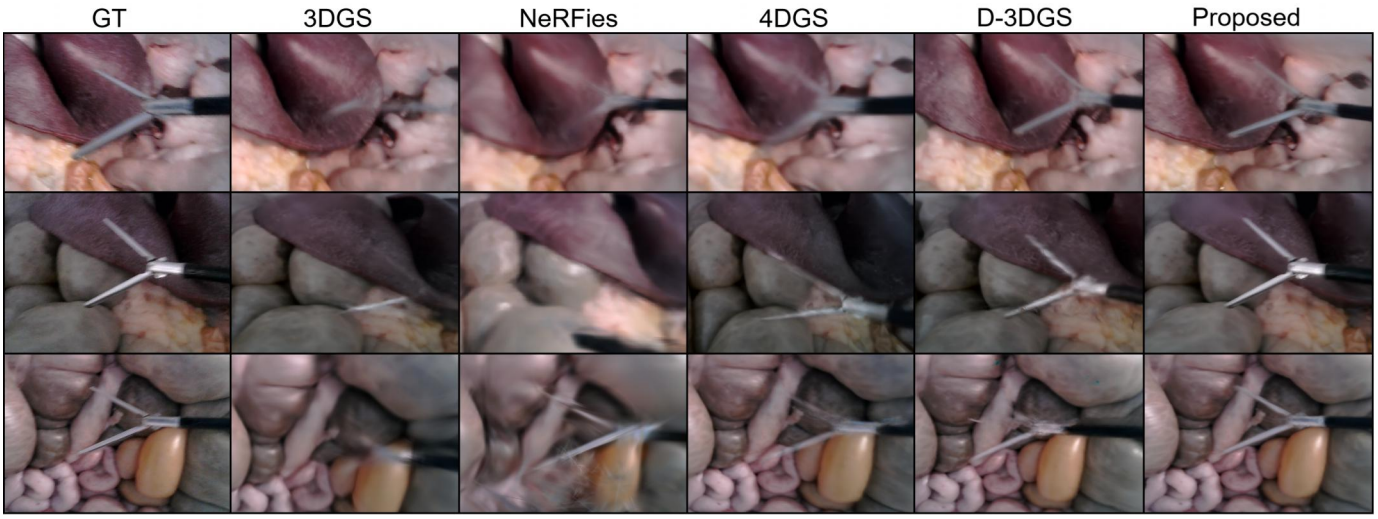

Fig. 7. Comparison of dynamic scene reconstruction using various methods. Each row represents the same training dataset, with the proposed method consistently showing more detailed reconstruction results, especially in the main body and jaw parts of the surgical instruments.

increase point cloud density but fail to correct errors caused by poor initialization, leading to the over-generation of Gaussian representations for the instruments. In contrast, (c) effectively manages density, preventing the spread of erroneous points and ensuring accurate Gaussian representation of the instruments (PSNR: (a) 15.76, (b) 14.21, (c) 17.33). Additionally, we visualize the effects of different rendering strategies on training. As shown in Figure 9, the absence of Dynamic Density Control (c) leads to extremely poor rendering quality, while the lack of Uniform Motion Rendering (d) results in inaccurate rendering of the surgical instruments (PSNR: (b) 28.31, (c) 15.42, (d) 22.26). Without Dynamic Density Control, our model had nearly an 80% chance of failing to complete the training in our preliminary experimentation when tuning the SfM settings,

TABLE II
DATA SOURCE COMPARISON ACROSS DIFFERENT MODEL TYPES (MEAN AND STANDARD DEVIATION)

Model	Metrics	REAL	AUGMENT [40]	D-3DGS [16]	4DGS [30]	**NeeCo**	**NeeCo + Real Images**
YOLOv5 [36]	Precision ↑	0.703 ± 0.007	0.731 ± 0.002	0.422 ± 0.009	0.476 ± 0.007	**0.694 ± 0.013**	**0.776 ± 0.011**
	Recall ↑	0.831 ± 0.003	0.852 ± 0.008	0.535 ± 0.011	0.557 ± 0.006	**0.826 ± 0.011**	**0.901 ± 0.015**
DBH-YOLO [38]	Precision ↑	0.712 ± 0.007	0.731 ± 0.004	0.501 ± 0.008	0.522 ± 0.006	**0.704 ± 0.011**	**0.826 ± 0.012**
	Recall ↑	0.721 ± 0.004	0.744 ± 0.007	0.501 ± 0.009	0.542 ± 0.008	**0.707 ± 0.008**	**0.829 ± 0.014**
U-Net [37]	IoU ↑	0.617 ± 0.008	0.622 ± 0.003	0.421 ± 0.015	0.447 ± 0.009	**0.601 ± 0.011**	**0.683 ± 0.012**
	Dice ↑	0.763 ± 0.004	0.767 ± 0.009	0.592 ± 0.012	0.617 ± 0.008	**0.751 ± 0.009**	**0.812 ± 0.013**
U-NetPlus [39]	IoU ↑	0.633 ± 0.006	0.652 ± 0.004	0.403 ± 0.013	0.426 ± 0.007	**0.627 ± 0.010**	**0.727 ± 0.013**
	Dice ↑	0.775 ± 0.004	0.789 ± 0.006	0.574 ± 0.009	0.597 ± 0.011	**0.771 ± 0.005**	**0.841 ± 0.011**

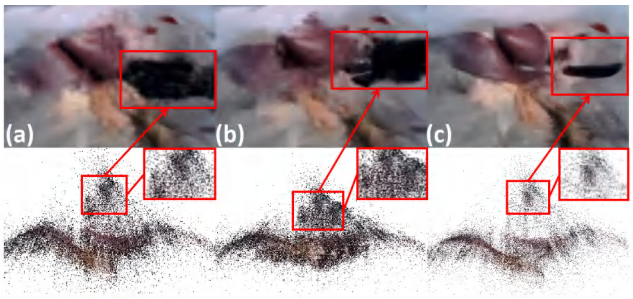

Fig. 8. Ablation study on Dynamic Density Control, indicating differences in Gaussian quality at 6k training iterations, (a) Kerbl et al. [13], (b) Zhang et al. [31] (c) Ours.

underscoring the importance of this method in our study.

2) Dynamic SH Update and Camera Pose Compensation: We compared the impact of Dynamic SH function updates and camera pose compensation on training. As shown in Table III, the model without any implementation yielded the poorest rendering quality. The model with only SH updates showed minial improvement in the early stages of training (4k-8k epochs) but demonstrated noticeable gains in the later stages (12k-20k epochs), as the early SH updates focused on lower orders, allowing the model to better address erroneous initializations. The model with Dynamic Camera Compensation exhibited consistent PSNR improvements throughout the training process. The best results were achieved when both methods were applied together.

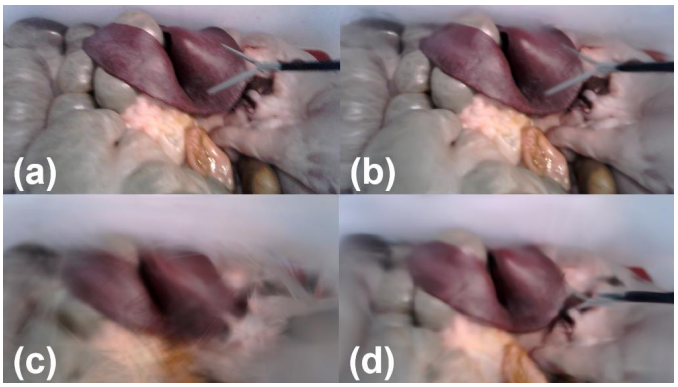

Fig. 9. (a) GT image, (b) results with both Dynamic Density Control and Uniform Motion Rendering applied, (c) without Dynamic Density Control, (d) without Uniform Motion Rendering.

TABLE III
ABLATION STUDY RESULTS

Metric	SH	Compensation	Epochs			
			4k	8k	12k	20k
PSNR↑	✗	✗	15.21	16.37	19.02	20.63
	✓	✗	15.34	16.77	20.64	22.53
	✗	✓	16.73	18.69	20.66	22.81
	✓	✓	**16.82**	**18.88**	**21.54**	**23.78**

V. CONCLUSION

This paper presents a novel pipeline for generating surgical instrument deformation images, which, compared to existing methods, contributes to creating realistic and diverse surgical image datasets. Our approach introduces dynamic 3D Gaussian models to represent the deformation of instruments in dynamic surgical scenes and employs a dynamic density control strategy to address the challenges posed by poor camera poses in real-world datasets, which often hinder training. Additionally, our method can generate annotation files, addressing the significant challenge of the lack of annotated data in medical imaging datasets. Our experiments demonstrate promising results, outperforming recent work and achieving object detection and segmentation performances that closely resemble those of models trained on GT imaging. Moreover, the datasets generated using our method's capability to render new deformations and viewpoints further surpass the performance of models trained solely on GT imaging. However, our method has limitations. It struggles to capture background tissue deformations accurately, particularly when such deformations follow a specific temporal or operational sequence. Our future work will address the challenge of predicting soft tissue deformations from unordered input and improving the recovery of these deformations.

REFERENCES

[1] P. Mascagni, D. Alapatt, L. Sestini, M. S. Altieri, A. Madani, Y. Watanabe, et al., "Computer vision in surgery: From potential to clinical value," *NPJ Digit. Med.*, vol. 5, no. 1, p. 163, Oct. 28 2022. DOI: 10.1038/s41746-022-00707-5

[2] S. Ramesh, V. Srivastav, D. Alapatt, T. Yu, A. Murali, L. Sestini, et al., "Dissecting self-supervised learning methods for surgical computer vision," *Med. Image Anal.*, vol. 88, p. 102844, Aug. 2023. DOI: 10.1016/j.media.2023.102844

[3] L. El Jiani, S. El Filali, and E. H. Benlahmer, "Overcome medical image data scarcity by data augmentation techniques: A review," in *2022 International Conference on Microelectronics (ICM)*, 2022, pp. 21–24. DOI: 10.1109/ICM56065.2022.10005544

[4] A. K. Upadhyay and A. K. Bhandari, "Advances in deep learning models for resolving medical image segmentation data scarcity problem: A topical review," *Arch. Comput. Methods Eng.*, vol. 31, no. 3, pp. 1701–1719, 2024. DOI: 10.1007/s11831-023-10028-9

[5] A. J. Lungu, W. Swinkels, L. Claesen, P. Tu, J. Egger, and X. Chen, "A review on the applications of virtual reality, augmented reality and mixed reality in surgical simulation: An extension to different kinds of surgery," *Expert Rev. Med. Devices*, vol. 18, no. 1, pp. 47–62, Jan. 2021. DOI: 10.1080/17434440.2021.1860750

[6] Y. Liu, Y. Tian, G. Maicas, L. Z. C. T. Pu, R. Singh, J. W. Verjans, et al., "Photoshopping colonoscopy video frames," in 2020 IEEE 17th International Symposium on Biomedical Imaging (ISBI). IEEE, 2020, pp. 1–5. DOI: 10.1109/ISBI45749.2020.9098406

[7] G. Luegmair, D. D. Mehta, J. B. Kobler, and M. Döllinger, "Three-dimensional optical reconstruction of vocal fold kinematics using high-speed video with a laser projection system," *IEEE Trans. Med. Imaging*, vol. 34, no. 12, pp. 2572–2582, Dec. 2015. DOI: 10.1109/TMI.2015.2445921

[8] N. Mahmoud, T. Collins, A. Hostettler, L. Soler, C. Doignon, and J. M. M. Montiel, "Live tracking and dense reconstruction for handheld monocular endoscopy," *IEEE Trans. Med. Imaging*, vol. 38, no. 1, pp. 79–89, Jan. 2019. DOI: 10.1109/TMI.2018.2856109

[9] L. C. Garcia-Peraza-Herrera, L. Fidon, C. D'Ettorre, D. Stoyanov, T. Vercauteren, and S. Ourselin, "Image compositing for segmentation of surgical tools without manual annotations," *IEEE Trans. Med. Imaging*, vol. 40, no. 5, pp. 1450–1460, May 2021. DOI: 10.1109/TMI.2021.3057884

[10] F. Fuentes-Hurtado, A. Kadkhodamohammadi, E. Flouty, S. Barbarisi, I. Luengo, and D. Stoyanov, "EasyLabels: Weak labels for scene segmentation in laparoscopic videos," *Int. J. Comput. Assist. Radiol. Surg.*, vol. 14, no. 7, pp. 1247–1257, Jul. 2019. DOI: 10.1007/s11548-019-02003-2

[11] J.-Y. Zhu, T. Park, P. Isola, and A. A. Efros, "Unpaired image-to-image translation using cycle-consistent adversarial networks," in *Proc IEEE/CVF Conf. on Computer Vision and Pattern Recognition*, 2017, pp. 2223–2232. DOI: 10.1109/ICCV.2017.244

[12] B. Mildenhall, P. P. Srinivasan, M. Tancik, J. T. Barron, R. Ramamoorthi, and R. Ng, "Nerf: Representing scenes as neural radiance fields for view synthesis," *Commun. ACM*, vol. 65, no. 1, pp. 99–106, 2021. DOI: 10.1145/3503250

[13] B. Kerbl, G. Kopanas, T. Leimkühler, and G. Drettakis, "3d gaussian splatting for real-time radiance field rendering," *ACM Trans. Graph.*, vol. 42, no. 4, pp. 1–14, 2023. DOI: 10.1145/3592433

[14] Y. Liu, C. Li, C. Yang, and Y. Yuan, "Endogaussian: Gaussian splatting for deformable surgical scene reconstruction," arXiv preprint *arXiv:*, 2024.

[15] Y. Wang, Y. Long, S. H. Fan, and Q. Dou, "Neural rendering for stereo 3d reconstruction of deformable tissues in robotic surgery," in *Proc. MICCAI 2022*. Springer, 2022, pp. 431–441. DOI: 10.1007/978-3-031-16449-1_41

[16] Z. Yang, X. Gao, W. Zhou, S. Jiao, Y. Zhang, and X. Jin, "Deformable 3d gaussians for high-fidelity monocular dynamic scene reconstruction," in *Proc IEEE/CVF Conf. on Computer Vision and Pattern Recognition*, 2024, pp. 20 331–20 341.

[17] O. Özyeşil, V. Voroninski, R. Basri, and A. Singer, "A survey of structure from motion*," *Acta Numer.*, vol. 26, pp. 305–364, 2017. DOI: 10.1017/S096249291700006X

[18] Y. Li, F. Richter, J. Lu, E. K. Funk, R. K. Orosco, J. Zhu, et al., "Super: A surgical perception framework for endoscopic tissue manipulation with surgical robotics," *IEEE Robot. Autom. Lett.*, vol. 5, no. 2, pp. 2294–2301, 2020. DOI: 10.1109/LRA.2020.2970659

[19] Y. Long, Z. Li, C. H. Yee, C. F. Ng, R. H. Taylor, M. Unberath, et al., "E-dssr: efficient dynamic surgical scene reconstruction with transformer-based stereoscopic depth perception," in *Proc. MICCAI 2021*. Springer, 2021, pp. 415–425. DOI: 10.1007/978-3-030-87202-1_40

[20] C. Yang, K. Wang, Y. Wang, X. Yang, and W. Shen, "Neural lerplane representations for fast 4d reconstruction of deformable tissues," in *Proc. MICCAI 2023*. Springer, 2023, pp. 46–56. DOI: 10.1007/978-3-031-43996-4_5

[21] L. Zhu, Z. Wang, Z. Jin, G. Lin, and L. Yu, "Deformable endoscopic tissues reconstruction with gaussian splatting," arXiv preprint *arXiv:*, 2024.

[22] J. Moore, H. Scheirich, S. Jadhav, A. Enquobahrie, B. Paniagua, A. Wilson, et al., "The interactive medical simulation toolkit (imstk): An open source platform for surgical simulation," *Front. Virtual Real.*, vol. 4, p. 1130156, 2023. DOI: 10.3389/frvir.2023.1130156

[23] S. Grossi, M. Cattoni, N. Rotolo, and A. Imperatori, "Video-assisted thoracoscopic surgery simulation and training: A comprehensive literature review," *BMC Med. Educ.*, vol. 23, no. 1, p. 535, Jul. 27 2023. DOI: 10.1186/s12909-023-04482-z

[24] M. Sahu, R. Strömsdörfer, A. Mukhopadhyay, and S. Zachow, "Endo-sim2real: Consistency learning-based domain adaptation for instrument segmentation," in *Proc. MICCAI 2020*. Springer, 2020, pp. 784–794. DOI: 10.1007/978-3-030-59716-0_75

[25] M. Sahu, A. Mukhopadhyay, and S. Zachow, "Simulation-to-real domain adaptation with teacher-student learning for endoscopic instrument segmentation," *Int. J. Comput. Assist. Radiol. Surg.*, vol. 16, no. 5, pp. 849–859, May 2021. DOI: 10.1007/s11548-021-02383-4

[26] Z. Zhang, B. Rosa, and F. Nageotte, "Surgical tool segmentation using generative adversarial networks with unpaired training data," *IEEE Robot. Autom. Lett.*, vol. 6, no. 4, pp. 6266–6273, 2021. DOI: 10.1109/LRA.2021.3092302

[27] E. Colleoni, D. Psychogyios, B. Van Amsterdam, F. Vasconcelos, and D. Stoyanov, ""Ssis-seg: Simulation-supervised image synthesis for surgical instrument segmentation," IEEE Trans. on Med," *IEEE Trans. Med. Imaging*, vol. 41, no. 11, pp. 3074–3086, Nov. 2022. DOI: 10.1109/TMI.2022.3178549

[28] P. M. Scheikl, E. Tagliabue, B. Gyenes, M. Wagner, D. Dall'Alba, P. Fiorini, et al., "Sim-to-real transfer for visual reinforcement learning of deformable object manipulation for robot-assisted surgery," *IEEE Robot. Autom. Lett.*, vol. 8, no. 2, pp. 560–567, 2023. DOI: 10.1109/LRA.2022.3227873

[29] J. L. Schonberger and J.-M. Frahm, "Structure-from-motion revisited," in *Proc IEEE/CVF Conf. on Computer Vision and Pattern Recognition*, 2016, pp. 4104–4113.

[30] G. Wu, T. Yi, J. Fang, L. Xie, X. Zhang, W. Wei, et al., "4d gaussian splatting for real-time dynamic scene rendering," in *Proc IEEE/CVF Conf. on Computer Vision and Pattern Recognition*, 2024, pp. 20 310–20 320.

[31] Z. Zhang, W. Hu, Y. Lao, T. He, and H. Zhao, "Pixel-gs: Density control with pixel-aware gradient for 3d gaussian splatting," arXiv preprint *arXiv:*, 2024.

[32] S. R. Bulò, L. Porzi, and P. Kontschieder, "Revising densification in gaussian splatting," arXiv preprint *arXiv:*, 2024.

[33] K. Park, U. Sinha, P. Hedman, J. T. Barron, S. Bouaziz, D. B. Goldman, et al., "Hypernerf: A higher-dimensional representation for topologically varying neural radiance fields," arXiv preprint *arXiv:*, 2021.

[34] O. Seiskari, J. Ylilammi, V. Kaatrasalo, P. Rantalankila, M. Turkulainen, J. Kannala, et al., "Gaussian splatting on the move: Blur and rolling shutter compensation for natural camera motion," arXiv preprint *arXiv:*, 2024.

[35] K. Park, U. Sinha, J. T. Barron, S. Bouaziz, D. B. Goldman, S. M. Seitz, et al., "Nerfies: Deformable neural radiance fields," in *Proc IEEE/CVF Conf. on Computer Vision and Pattern Recognition*, 2021, pp. 5865–5874.

[36] J. Redmon, S. Divvala, R. Girshick, and A. Farhadi, "You only look once: Unified, real-time object detection," in *Proc IEEE/CVF Conf. on Computer Vision and Pattern Recognition*, 2016, pp. 779–788. DOI: 10.1109/CVPR.2016.91

[37] O. Ronneberger, P. Fischer, and T. Brox, "U-net: Convolutional networks for biomedical image segmentation," in *Proc. MICCAI 2015*. Springer, 2015, pp. 234–241. DOI: 10.1007/978-3-319-24574-4_28

[38] X. Pan, M. Bi, H. Wang, C. Ma, and X. He, "DBH-YOLO: A surgical instrument detection method based on feature separation in laparoscopic surgery," *Int. J. Comput. Assist. Radiol. Surg.*, vol. •••, pp. 1–11, Apr. 13 2024. DOI: 10.1007/s11548-024-03115-0

[39] S. K. Hasan and C. A. Linte, "U-netplus: A modified encoder-decoder u-net architecture for semantic and instance segmentation of surgical instruments from laparoscopic images," in *Proc. IEEE Int. Conf. EMBC 2019* . IEEE, 2019, pp. 7205–7211.

[40] A. Mikołajczyk and M. Grochowski, "Data augmentation for improving deep learning in image classification problem," in 2018 Int. Interdisciplinary PhD Workshop (IIPhDW). IEEE, 2018, pp. 117–122. DOI: 10.1109/IIPHDW.2018.8388338